

# First *in vivo* and phantom imaging of cyclotron produced $^{133}\text{La}$ as a theranostic radionuclide for $^{225}\text{Ac}$ and $^{135}\text{La}$

Bryce J.B. Nelson<sup>1</sup>, Simon Ferguson<sup>1</sup>, Melinda Wuest<sup>1,2</sup>, John Wilson<sup>1</sup>, M. John M. Duke<sup>1</sup>,  
Susan Richter<sup>1,2</sup>, Hans Soenke-Jans<sup>1,2</sup>, Jan D. Andersson<sup>1,3</sup>, Freimut Juengling<sup>1</sup>, Frank Wuest<sup>1,2\*</sup>

<sup>1</sup> Department of Oncology, Cross Cancer Institute, University of Alberta, 11560 University Ave,  
Edmonton AB, T6G 1Z2, Canada

<sup>2</sup> Cancer Research Institute of Northern Alberta (CRINA), University of Alberta, Edmonton, AB,  
T6G 2S2, Canada

<sup>3</sup> Edmonton Radiopharmaceutical Center, Cross Cancer Institute, Alberta Health Services, 11560  
University Ave, Edmonton AB, T6G 1Z2, Canada

**Running title:** Preclinical and Phantom Imaging of  $^{133}\text{La}$

## KEYWORDS

PET, Radiolanthanum, Actinium-225, Theranostics, Cyclotron

\*Corresponding author at: Department of Oncology, University of Alberta, 11560  
University Avenue, Edmonton, AB T6G 1Z2, Canada.  
Tel.: +1-780-391-7666;  
Fax: +1-780-432-8483.  
E-mail address: wuest@ualberta.ca (F. Wuest).

**Immediate Open Access:** Creative Commons Attribution 4.0 International License (CC BY)  
allows users to share and adapt with attribution, excluding materials credited to previous  
publications.

License: <https://creativecommons.org/licenses/by/4.0/>.

Details: <https://jnm.snmjournals.org/page/permissions>.



## ABSTRACT

Theranostic isotope pairs have gained recent clinical interest as they can be labeled to the same tracer and applied for diagnostic and therapeutic purposes. The goals of this study were to A) investigate cyclotron production of clinically relevant  $^{133}\text{La}$  activities using natural and isotopically enriched barium target material, B) compare fundamental positron emission tomography (PET) phantom imaging characteristics of  $^{133}\text{La}$  with common PET radionuclides, and C) demonstrate *in vivo* preclinical PET tumor imaging using  $^{133}\text{La}$ -PSMA-I&T.

**Methods:**  $^{133}\text{La}$  was produced on a 24 MeV cyclotron using an aluminum-indium sealed target with 150-200 mg of isotopically enriched  $^{135}\text{BaCO}_3$ ,  $^{\text{nat}}\text{BaCO}_3$ , and  $^{\text{nat}}\text{Ba}$  metal. A NEPTIS Mosaic-LC performed Ba/La separation. DOTA, PSMA-I&T, and macropa were radiolabeled with  $^{133}\text{La}$ . Derenzo and National Electrical Manufacturers Association (NEMA) phantom imaging was performed with  $^{133}\text{La}$ ,  $^{132}\text{La}$ , and  $^{89}\text{Zr}$  and compared with  $^{18}\text{F}$ ,  $^{68}\text{Ga}$ ,  $^{44}\text{Sc}$ , and  $^{64}\text{Cu}$ . *In vivo* preclinical imaging was performed with  $^{133}\text{La}$ -PSMA-I&T in LNCaP tumor-bearing mice.

**Results:** Proton irradiations for 100  $\mu\text{A}\cdot\text{min}$  at 23.3 MeV yielded  $214 \pm 7$  MBq  $^{133}\text{La}$  and  $28 \pm 1$  MBq  $^{135}\text{La}$  using  $^{135}\text{BaCO}_3$ ,  $59 \pm 2$  MBq  $^{133}\text{La}$  and  $35 \pm 1$  MBq  $^{135}\text{La}$  using  $^{\text{nat}}\text{BaCO}_3$  and  $81 \pm 3$  MBq  $^{133}\text{La}$  and  $48 \pm 1$  MBq  $^{135}\text{La}$  using  $^{\text{nat}}\text{Ba}$  metal. At 11.9 MeV,  $^{135}\text{La}$  yields were:  $81 \pm 2$  MBq,  $6.8 \pm 0.4$  MBq, and  $9.9 \pm 0.5$  MBq for  $^{135}\text{BaCO}_3$ ,  $^{\text{nat}}\text{BaCO}_3$ , and  $^{\text{nat}}\text{Ba}$  metal.  $\text{BaCO}_3$  target material recovery was  $95.4 \pm 1.7\%$ . NEMA and Derenzo phantom imaging demonstrated  $^{133}\text{La}$  PET spatial resolution, and scanner recovery coefficient were superior compared to  $^{68}\text{Ga}$ ,  $^{132}\text{La}$ , and comparable to  $^{89}\text{Zr}$ . The apparent molar activity was  $130 \pm 15$  GBq/ $\mu\text{mol}$  with DOTA,  $73 \pm 18$  GBq/ $\mu\text{mol}$  with PSMA-I&T, and  $206 \pm 31$  GBq/ $\mu\text{mol}$  with macropa. Preclinical PET imaging with  $^{133}\text{La}$ -PSMA-I&T provided high-resolution tumor visualization with a  $\text{SUV}_{60\text{min}}$  of  $0.97 \pm 0.17$ .

**Conclusions:** With high-yield  $^{133}\text{La}$  cyclotron production, recovery of  $\text{BaCO}_3$  target material, and superior fundamental imaging characteristics compared to  $^{68}\text{Ga}$  and  $^{132}\text{La}$ ,  $^{133}\text{La}$  represents a promising radiometal candidate to provide high-resolution PET imaging as a PET/alpha therapy theranostic pair with  $^{225}\text{Ac}$ , or a PET/Auger electron therapy theranostic pair with  $^{135}\text{La}$ .

## INTRODUCTION

Theranostic pairs in nuclear medicine involve labeling molecular target vectors first with a diagnostic radionuclide, followed by a therapeutic particle emitting radionuclide (1). Both radionuclides should have similar chemical properties, ideally being isotopes of the same element. Theranostics has strong potential in targeted radionuclide therapy, where a diagnostic positron or gamma-emitting radionuclide used in PET or SPECT is paired with an alpha ( $\alpha$ ), beta ( $\beta^-$ ), or Auger electron-emitting therapeutic radionuclide (2). Recently introduced  $^{133}\text{La}$  ( $t_{1/2}=3.9$  h),  $^{132}\text{La}$  ( $t_{1/2}=4.8$  h), and  $^{134}\text{Ce}$  ( $t_{1/2}=3.2$  d)/ $^{134}\text{La}$  ( $t_{1/2}=6.5$  min) PET radionuclides are uniquely suited as theranostic imaging partners for  $^{225}\text{Ac}$  ( $t_{1/2}=9.9$  d) in targeted alpha therapy (TAT), or with  $^{135}\text{La}$  ( $t_{1/2}=19.5$  h) in Auger electron therapy (AET) due to their chemical similarity and longer half-lives compared to the ubiquitous PET radiometal  $^{68}\text{Ga}$  ( $t_{1/2}=68$  min) (2-7). Actinium-225 has shown considerable efficacy in clinical trials for treating metastatic cancers (2,8). Lanthanum-132 has been proposed as a theranostic PET imaging surrogate for  $^{225}\text{Ac}$  therapy, and displayed similar *in vivo* uptake characteristics compared to  $^{225}\text{Ac}$  (6). However, there are fundamental imaging limitations inherent to  $^{132}\text{La}$  due to its high positron emission energy ( $E_{\text{max}}/E_{\text{mean}}=3.67/1.29$  MeV) that significantly reduces image spatial resolution and contrast compared to other PET radionuclides (e.g.  $^{18}\text{F}$   $E_{\text{max}}/E_{\text{mean}}=0.634/0.250$  MeV,  $^{68}\text{Ga}$   $E_{\text{max}}/E_{\text{mean}}=1.90/0.829$  MeV,  $^{64}\text{Cu}$   $E_{\text{max}}/E_{\text{mean}}=0.653/0.278$  MeV,  $^{44}\text{Sc}$   $E_{\text{max}}/E_{\text{mean}}=1.47/0.632$  MeV), and high energy and intensity gamma emissions that are problematic from a dosimetric perspective (3,9).  $^{133}\text{La}$  has a lower positron emission energy ( $E_{\text{max}}/E_{\text{mean}}=1.02/0.461$  MeV) than  $^{132}\text{La}$ ,  $^{68}\text{Ga}$ ,  $^{44}\text{Sc}$ , comparable energy to  $^{89}\text{Zr}$  ( $E_{\text{max}}/E_{\text{mean}}=0.902/0.396$  MeV), and lower energy and intensity gamma emissions than  $^{89}\text{Zr}$ ,  $^{44}\text{Sc}$ , and  $^{132}\text{La}$  (3). Here, as outlined in Figure 1, we describe a high yield cyclotron production method for  $^{133}\text{La}$  using natural and isotopically enriched  $^{135}\text{BaCO}_3$ , phantom measurements

comparing fundamental imaging properties of  $^{133}\text{La}$  to other PET radionuclides including  $^{18}\text{F}$ ,  $^{68}\text{Ga}$ ,  $^{64}\text{Cu}$ ,  $^{89}\text{Zr}$ ,  $^{44}\text{Sc}$ ,  $^{132}\text{La}$ , and the first preclinical PET imaging with  $^{133}\text{La}$ . We have chosen to radiolabel PSMA-I&T for imaging prostate cancers.

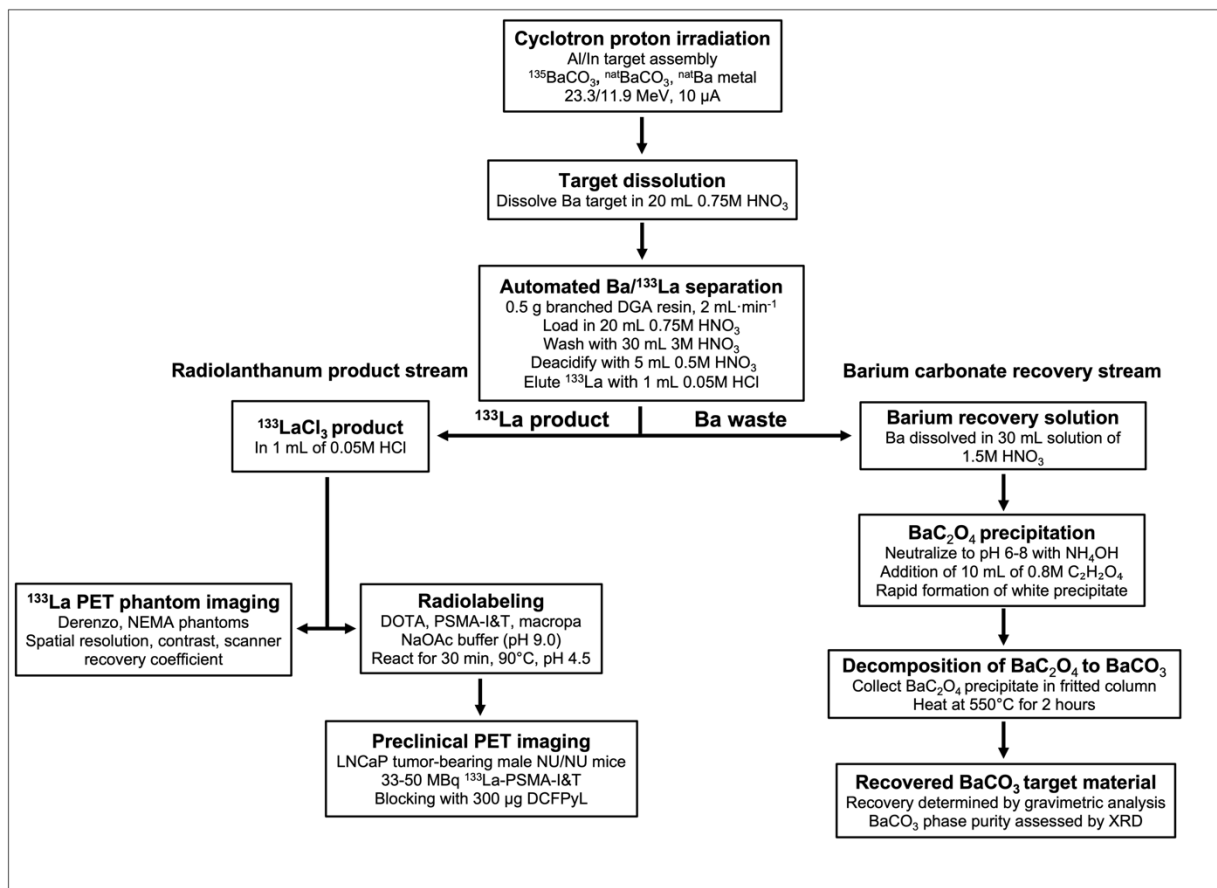


FIGURE 1. Experimental overview.

## MATERIALS AND METHODS

### Chemicals

Table 1 displays the isotopic compositions of  $^{135}\text{BaCO}_3$ ,  $^{\text{nat}}\text{BaCO}_3$ , and  $^{\text{nat}}\text{Ba}$  metal. Isotopically enriched  $^{135}\text{BaCO}_3$  was obtained from Trace Sciences International. Barium carbonate (99.999% trace metals basis), barium metal (99.99% trace metals basis), ACS reagent grade concentrated hydrochloric acid (37%), nitric acid (70%), ammonium hydroxide (28%), and periodic table mix inductively-coupled plasma optical emission spectrometry (ICP-OES) elemental standards were obtained from Sigma-Aldrich. Oxalic acid dihydrate (99.5%) was purchased from Fisher Scientific. Aluminum discs were obtained from Michaels, and aluminum foil was purchased from Goodfellow Cambridge. Indium wire was purchased from AIM Specialty Materials. Branched DGA resin was purchased from Eichrom. Eckert & Ziegler Isotopes NIST traceable  $\gamma$ -ray sources were used for high-purity germanium detector (HPGe) energy and efficiency calibration. Thin-layer chromatography silica gel sheets were purchased from Merck. 18 M $\Omega$ -cm water was obtained from a MilliporeSigma Direct-Q<sup>®</sup> 3 UV system.  $^{89}\text{Zr}$  was provided by the Washington University Cyclotron Facility in St. Louis, Mo. DOTA was purchased from Macrocyclics. Macropa was purchased from MedChemExpress. PSMA-I&T was obtained from ABX advanced biochemical compounds. DCFPyL was synthesized in-house.

### Instrumentation

Activity and radionuclidic purity were assessed using an ORTEC GEM35P4-70-SMP high-purity germanium detector running GammaVision software, with dead times below 25%. Elemental purity was assessed using an Agilent Technologies 720 Series ICP-OES. An Optimized

Radiochemical Applications NEPTIS Mosaic-LC synthesis unit separated  $^{133}\text{La}$  from the Ba target solution.

An Eckert & Ziegler AR-2000 Radio-TLC Imaging Scanner quantified the fraction of chelator-bound  $^{133}\text{La}$  after reaction. Solid targets were manufactured using a Carver Model 6318 hydraulic press and a MTI Corporation 10 mm (I.D.) EQ-Die-10D-B hardened steel die. A Carbolite TZF 16/610 tube furnace was used for  $^{135}\text{BaCO}_3$  recovery. X-ray powder diffraction (XRD) patterns were acquired on starting and recovered  $\text{BaCO}_3$  and intermediate  $\text{BaC}_2\text{O}_4$  using a Rigaku Ultima IV X-ray diffractometer to confirm phase identity and purity.

### **Cyclotron Targetry and Irradiation**

Figure 2 depicts nuclear reaction cross-sections for the  $^{13x}\text{Ba}(p,xn)^{13x}\text{La}$  reactions of interest for  $^{132/133/135}\text{La}$  production from the TENDL 2019 library, weighted for  $^{\text{nat}}\text{Ba}$  and isotopically enriched  $^{135}\text{BaCO}_3$  target material (10). Cyclotron targets were prepared with 150-200 mg of  $^{\text{nat}}\text{Ba}$  metal,  $^{\text{nat}}\text{BaCO}_3$ , or enriched  $^{135}\text{BaCO}_3$ , a roughened aluminum disc (24 mm diameter, 1.35 mm thick), indium wire (1 mm diameter), and aluminum foil (125  $\mu\text{m}$  thick) in a manner similar to that previously described (3,11). Aluminum was shown to be an adequate substitution for silver, presenting a lower cost and activation. Target components are shown in supplemental Figure 1. Targets were irradiated for 5-263 minutes at 11.9 and 23.3 MeV using an Advanced Cyclotron Systems Inc. TR-24 cyclotron, at proton beam currents of 10  $\mu\text{A}$  incident on the target assembly. Higher energy runs (beam extracted at 24 MeV, 23.3 MeV incident on target pellets, 20.2 MeV exiting Ba metal, 19.4 MeV exiting  $\text{BaCO}_3$ ) were performed with 200 mg of Ba material with the aluminum target cover facing the beam, to maximize  $^{133}\text{La}$  production based on TENDL 2019 cross-section simulation data (10). During higher energy runs, a silver disc was placed behind

the target to avoid  $^{13}\text{N}$  production from the  $^{16}\text{O}(p,\alpha)^{13}\text{N}$  reaction. For lower energy runs (18.2 MeV extraction, 11.9 MeV incident on target pellets, 7.8 MeV exiting Ba metal, 6.4 MeV exiting  $\text{BaCO}_3$ ), performed to maximize  $^{135}\text{La}$  production, 150 mg Ba material was used, and the target was installed in reverse with the aluminum disc acting as a degrader to reduce beam energy from 18.2 MeV to 11.9 MeV, as calculated using SRIM (12).

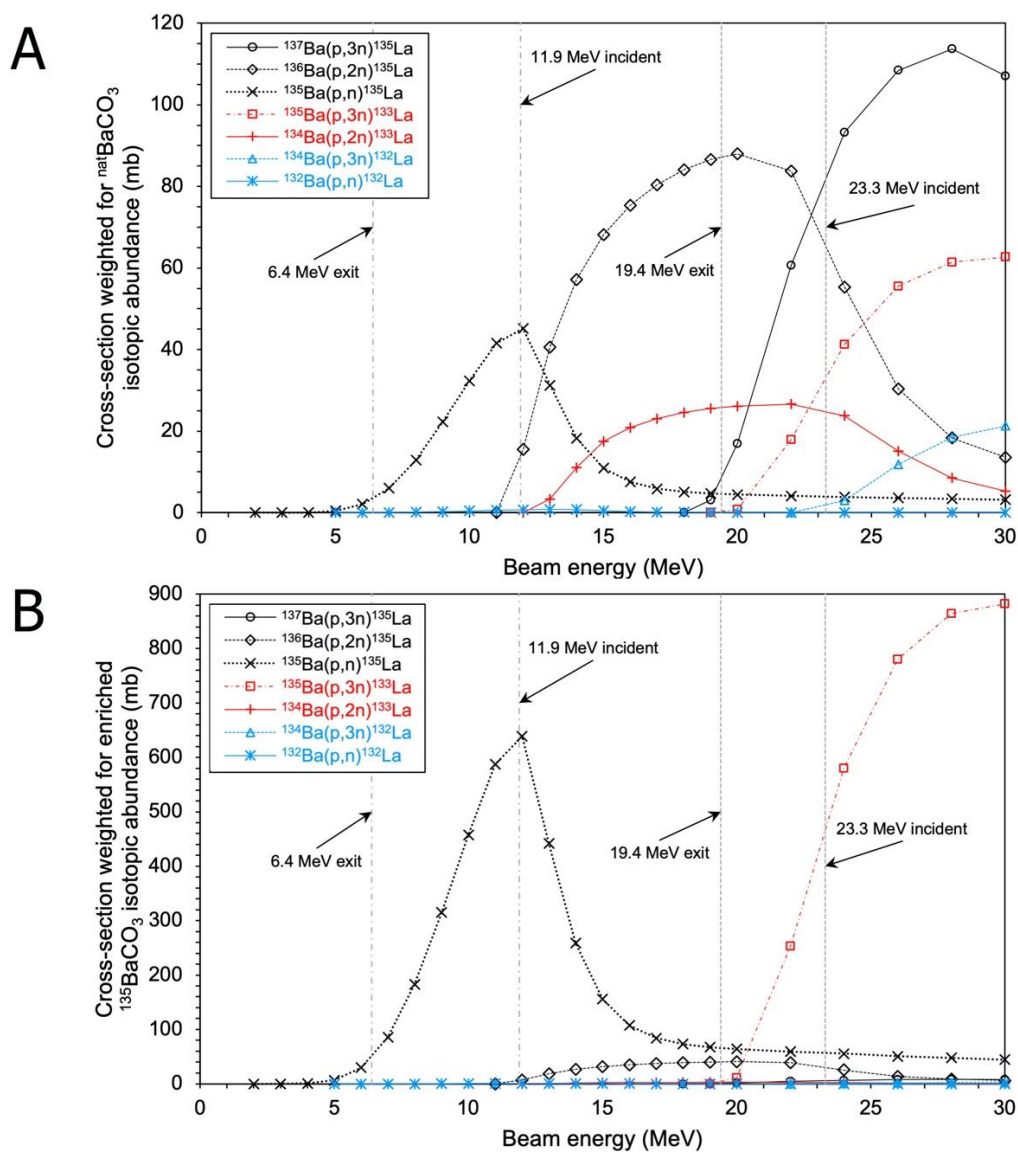


**FIGURE 2.** Nuclear reaction cross-section simulation data of the proton-induced nuclear reactions on  $^{132/134/135/136/137}\text{Ba}$  for  $^{132/133/135}\text{La}$  production weighted for (A)  $^{\text{nat}}\text{Ba}$  isotopic abundance and (B) isotopically enriched  $^{135}\text{BaCO}_3$  abundance (10).

## **Automated $^{133}\text{La}$ Separation and Radiochemical Purity Analysis**

$^{133}\text{La}$  and  $\text{BaCO}_3$  were separated using a process with aspects derived from previous studies (3,4). The target was opened by peeling back the aluminum cover, and placed in a Teflon dissolution vessel. The vessel was filled with 10 mL of 18 M $\Omega$ ·cm water, and sonicated in an ultrasonic bath for 3 min to dislodge the  $\text{BaCO}_3$  from the target backing. Target components were removed, rinsed with 5 mL of 18 M $\Omega$ ·cm water into the vessel, and 5 mL of 3M  $\text{HNO}_3$  was added, resulting in a 0.75M  $\text{HNO}_3$  reaction mixture that dissolved the  $\text{BaCO}_3$  in 5 min. This solution was passed through a SPE cartridge containing 0.50 g of branched DGA resin (conditioned with 10 mL 3M  $\text{HNO}_3$ ), and washed with 50 mL of 3M  $\text{HNO}_3$  to remove residual Ba and other metal impurities, followed by column deacidification with 5 mL of 0.5M  $\text{HNO}_3$ . Flow rates were kept below 2 mL·min<sup>-1</sup> to avoid  $^{133}\text{La}$  loss from the resin.  $^{133}\text{LaCl}_3$  was eluted using 1 mL of 0.05M  $\text{HCl}$ . After passing through the resin, the first 30 mL of process solution was diverted to a collection vial for subsequent  $\text{BaCO}_3$  recovery. After separation, target components were sonicated in 18 M $\Omega$ ·cm water for reuse. Radionuclidic and elemental purity of  $^{133}\text{LaCl}_3$  was determined by HPGe gamma-ray spectroscopy and ICP-OES.

## **$\text{BaCO}_3$ Target Material Recovery**

The 30 mL barium recovery solution was neutralized to pH 6-8 with  $\text{NH}_4\text{OH}$ . 10 mL of 0.8M  $\text{C}_2\text{H}_2\text{O}_4$  was added to the recovery solution to precipitate  $\text{BaC}_2\text{O}_4$ . The solution was passed through a fritted column to trap  $\text{BaC}_2\text{O}_4$ , and washed with 50 mL of 18 M $\Omega$ ·cm water.  $\text{BaC}_2\text{O}_4$  was removed from the column, then heated to 550°C for two hours in a sealed tube furnace with an airflow of 20 mL/min to decompose  $\text{BaC}_2\text{O}_4$  to  $\text{BaCO}_3$ , while avoiding conversion to  $\text{BaO}$  (13). Waste gases from decomposition were vented to a fume hood. Recovery was quantified by

gravimetric analysis of dried samples, and tracked by HPGe gamma spectroscopy using gamma emissions from  $^{135\text{m}}\text{Ba}$  (268 keV,  $t_{1/2}=28.7$  h). Samples of purchased  $\text{BaCO}_3$ , precipitated  $\text{BaC}_2\text{O}_4$ , and recovered  $\text{BaCO}_3$  were analyzed by XRD to evaluate product identification and quality.

### **Phantom Imaging**

Phantom imaging was performed using Derenzo and National Electrical Manufacturers Association (NEMA) Image quality phantoms on an INVEON<sup>®</sup> PET/CT scanner (Siemens Preclinical Solutions), as described by Ferguson et al. (14). The Derenzo phantom, used to investigate image contrast and spatial resolution, consists of sections with rods of varying diameters (0.8, 1.0, 1.25, 1.5, 2.0, and 2.5 mm) that are filled with the radionuclide of interest diluted in 20-30 mL of water. The NEMA phantom, used to investigate image noise, spill-over ratio (SOR), and recovery coefficient (RC), consists of several fillable sections including two 7.5 mm diameter cold air and water cylindrical volumes. NEMA and Derenzo Phantom scans for  $^{133}\text{La}$ ,  $^{132}\text{La}$ , and  $^{89}\text{Zr}$  were acquired in list mode, binned into sinograms and reconstructed with the default FBP (filtered back projection), OSEM (ordered subset expectation maximization) and MAP (maximum a posteriori estimation) algorithms. Acquisition, data processing and evaluation followed the same procedure as used by Ferguson et al. (14) for  $^{18}\text{F}$ ,  $^{64}\text{Cu}$ ,  $^{68}\text{Ga}$ , and  $^{44}\text{Sc}$  to enable direct comparison of the different radionuclides' imaging performance.

### **Radiolabeling of DOTA, PSMA-I&T, and macropa with $^{133}\text{La}$**

Similar to techniques in previous studies (3,4), the activity of a 500  $\mu\text{L}$   $^{133}\text{LaCl}_3$  aliquot was measured, and the solution pH was adjusted to 4.5 with 50  $\mu\text{L}$  of NaOAc buffer (pH 9.0). 100  $\mu\text{L}$  of this  $^{133}\text{La}$  solution (5 to 150 MBq) was reacted with 0.1-20  $\mu\text{g}$  of DOTA, PSMA-I&T,

and macropa dissolved in 50  $\mu\text{L}$  of 18  $\text{M}\Omega\cdot\text{cm}$  water at  $90^\circ\text{C}$  for 30 min. Each solution was analyzed using radio-TLC on silica plates to determine radiochemical purity and incorporation with 0.1 M citric acid buffer as the mobile phase.

### **Preclinical PET Imaging**

Animal studies using LNCaP tumor-bearing male NU/NU Nude mice (Charles River Laboratories) were carried out according to the guidelines of the Canadian Council on Animal Care (CCAC) and approved by the local Cross Cancer Institute Animal Care Committee. Static PET image scans (20 min duration) of  $^{133}\text{La}$ -PSMA-I&T at 60 min p.i. were performed on an INVEON<sup>®</sup> PET/CT scanner (Siemens Preclinical Solutions). Blocking experiments were performed using the PSMA-targeting agent DCFPyL. Radiotracer (33-50 MBq  $^{133}\text{La}$ -PSMA-I&T in 80-120  $\mu\text{L}$  of NaOAc/saline) and blocking compound (300  $\mu\text{g}$  DCFPyL, 5 min pre-dosed) were injected into the tail vein of isoflurane-anesthetized mice (100% oxygen; gas flow 1.5 L/min), mice were placed in a prone position into the center of the field of view, and body temperature was kept constant at  $37^\circ\text{C}$ . A transmission scan for attenuation correction was not acquired. The frames were reconstructed using ordered subset expectation maximization (OSEM) and maximum a posteriori (MAP) algorithms. No correction for partial volume effects was applied. The image files were processed using the ROVER v2.0.51 software (ABX GmbH).

### **Statistical Analysis**

All data are given as mean  $\pm$  standard deviation, for  $n \geq 3$ .

## RESULTS

### Cyclotron Targetry and Irradiation

Average EOB activities (n=3) of  $^{133}\text{La}$  and co-produced  $^{135}\text{La}$  for 100  $\mu\text{A}\cdot\text{min}$  runs (10  $\mu\text{A}$  for 10 min) at 11.9 and 23.3 MeV beam energies with different barium target materials are summarized in Table 2. Irradiating enriched  $^{135}\text{BaCO}_3$  at 23.3 MeV resulted in a significant increase in  $^{133}\text{La}$  production compared to  $^{\text{nat}}\text{BaCO}_3$  and  $^{\text{nat}}\text{Ba}$  metal. Irradiating recovered  $^{\text{nat}}\text{BaCO}_3$  at 23.3 MeV for 100  $\mu\text{A}\cdot\text{min}$  yielded  $57 \pm 1$  MBq  $^{133}\text{La}$  and  $36 \pm 1$  MBq  $^{135}\text{La}$ , similar to yields for fresh  $^{\text{nat}}\text{BaCO}_3$ .

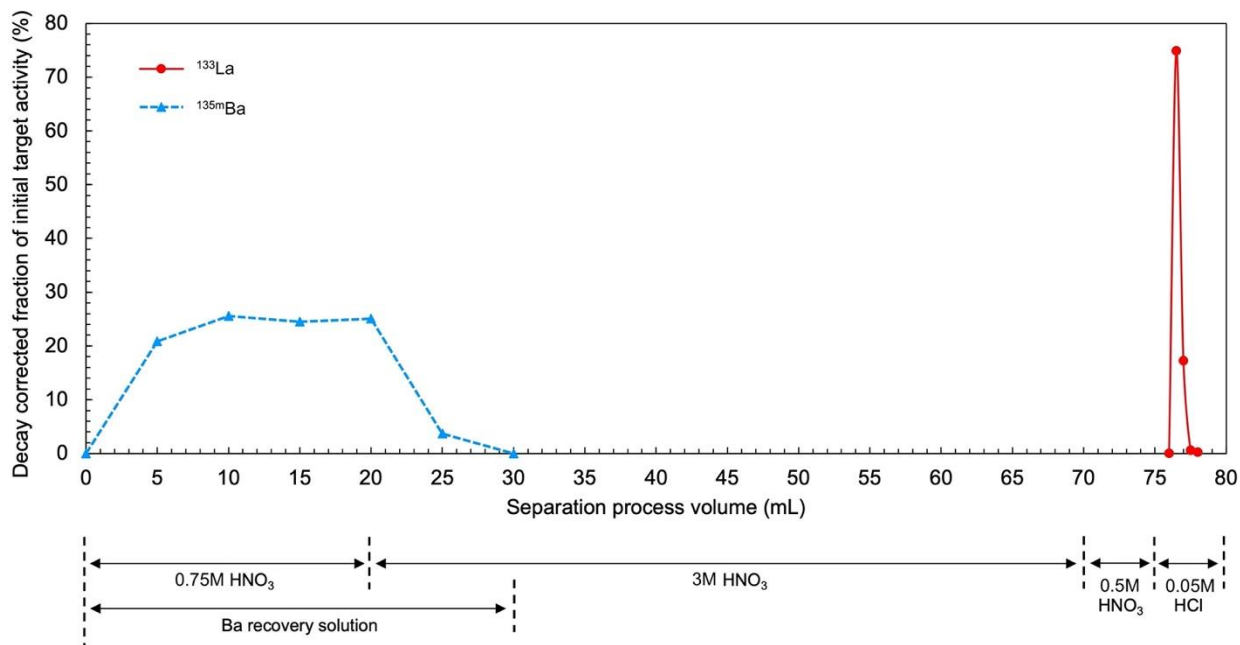
### $^{133}\text{La}$ Separation and Radiochemical Purity Analysis

Table 3 contains ICP-OES elemental purity results for the  $^{133}\text{LaCl}_3$  product. After removal from the reactor post-sonification, the aluminum target backing and cover contained no detectable  $^{133}\text{La}$  activity. The entire separation took ~50 min. Over 92% of decay-corrected  $^{133}\text{La}$  was recovered in 1 mL of 0.05M HCl, and HPGe analysis of the  $^{133}\text{LaCl}_3$  product produced with  $^{\text{nat}}\text{BaCO}_3$  showed small activities of  $^{131}\text{La}$  ( $t_{1/2}=59$  min) and  $^{132}\text{La}$  ( $t_{1/2}=4.8$  h) with no other observed radionuclidic impurities, similar to (3).  $^{131}\text{La}$  and  $^{132}\text{La}$  were not observed in  $^{133}\text{LaCl}_3$  produced with isotopically enriched  $^{135}\text{BaCO}_3$ . Elemental purity determined by ICP-OES of  $^{133}\text{LaCl}_3$  produced with fresh and recovered  $\text{BaCO}_3$  target material was superior to  $^{133}\text{LaCl}_3$  previously produced with Ba metal in (3).

### Enriched $^{135}\text{BaCO}_3$ Recovery

Figure 3 depicts the decay corrected fraction of total  $^{135\text{m}}\text{Ba}$  and  $^{135}\text{La}$  activity as a function of process volume. The solution was collected in fractions (5 mL for 0-75 mL, 0.5 mL for 75-80

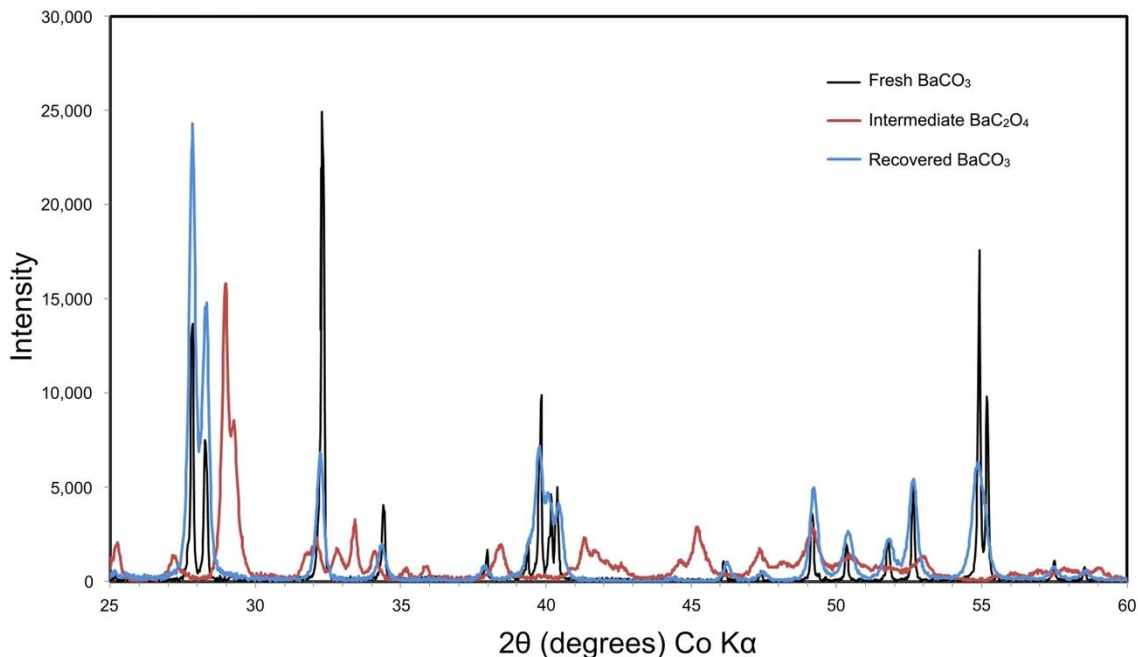
mL) after flowing through the resin, and each fraction was analyzed on the HPGe to quantify  $^{135\text{m}}\text{Ba}$  and  $^{135}\text{La}$  activity via their respective 268 and 481 keV gamma emissions. Over 99.7% of decay-corrected  $^{135\text{m}}\text{Ba}$  activity was recovered in the first 6 fractions with no detectable contributions from additional fractions, so only the first 30 mL of process solution was collected for recovery.



**FIGURE 3.** Decay corrected fraction of initial  $^{135\text{m}}\text{Ba}$  and  $^{135}\text{La}$  target activity in SPE cartridge eluate as a function of process volume.

$\text{BaC}_2\text{O}_4$  formed a white precipitate and was collected by the fritted column. Following  $\text{BaC}_2\text{O}_4$  thermal decomposition to  $\text{BaCO}_3$  from heating at  $550^\circ\text{C}$ , gravimetric analysis indicated a recovery of  $191.1 \pm 3.2$  mg, which for a  $200.3 \pm 0.3$  mg initial target pellet mass corresponds to a  $\text{BaCO}_3$  recovery of  $95.4 \pm 1.7\%$  ( $n=3$ ).

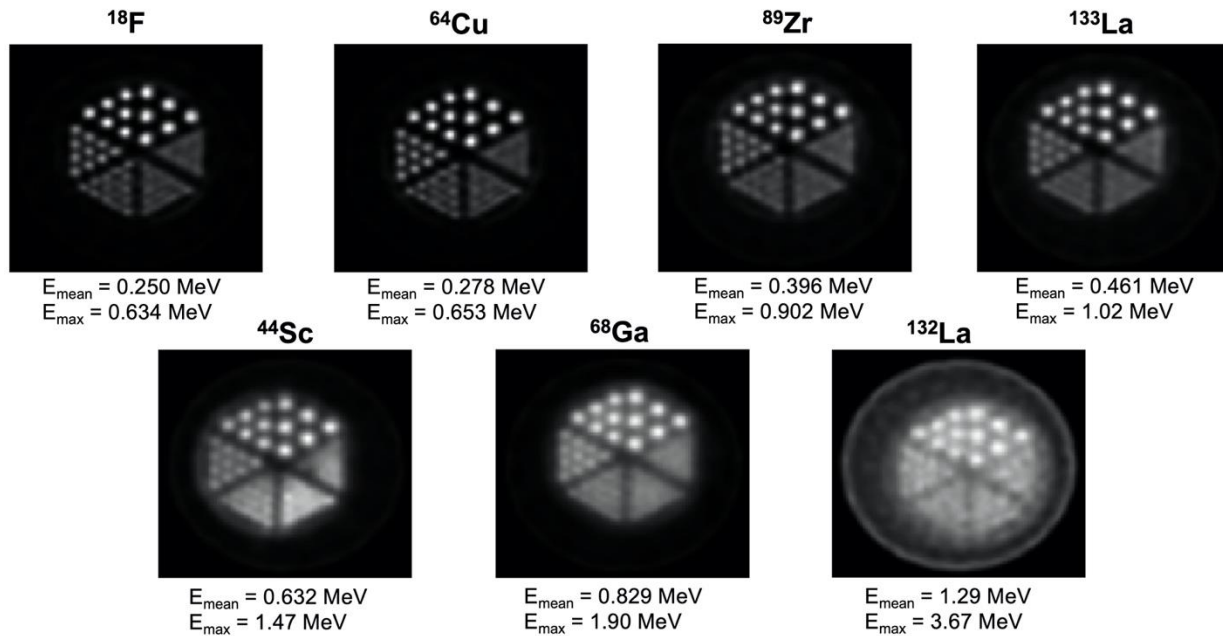
Figure 4 depicts the XRD diffractograms acquired for fresh BaCO<sub>3</sub>, intermediate BaC<sub>2</sub>O<sub>4</sub>, and recovered BaCO<sub>3</sub> material. Complete XRD diffractogram data are in supplemental Tables 1-3 and supplemental Figures 2-4. The absence of unexplained reflections in all three patterns compared to standard reference lines confirmed the high phase purity of the compounds and the complete conversion of BaC<sub>2</sub>O<sub>4</sub> to BaCO<sub>3</sub> (15).



**FIGURE 4.** Background stripped XRD diffractograms of fresh BaCO<sub>3</sub>, intermediate BaC<sub>2</sub>O<sub>4</sub>, and recovered BaCO<sub>3</sub>.

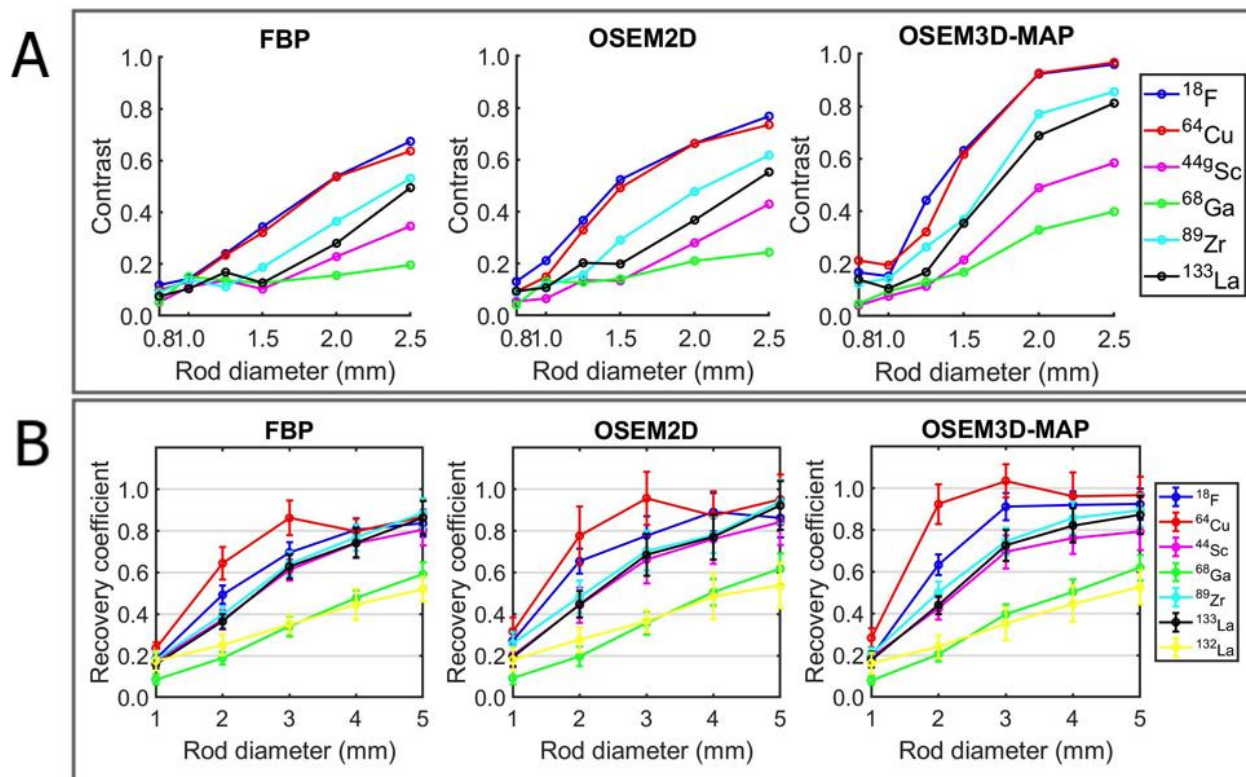
### Phantom Imaging

Figure 5 depicts Derenzo phantom scans with the mean and maximum positron energies of <sup>133</sup>La, <sup>132</sup>La and other commonly used PET radionuclides. Derenzo phantom scans acquired with <sup>18</sup>F, <sup>64</sup>Cu, <sup>89</sup>Zr, <sup>133</sup>La, <sup>44</sup>Sc, <sup>68</sup>Ga, and <sup>132</sup>La clearly show that lower mean and maximum positron energies improve PET image spatial resolution and contrast. <sup>133</sup>La exhibits similar spatial resolution to <sup>89</sup>Zr, is an improvement over <sup>44</sup>Sc and <sup>68</sup>Ga, and is superior to <sup>132</sup>La.



**FIGURE 5.** Derenzo phantom images reconstructed with MAP for different PET radionuclides, presented in order of increasing positron emission energy.  $^{18}\text{F}$ ,  $^{64}\text{Cu}$ ,  $^{44}\text{Sc}$  and  $^{68}\text{Ga}$  data were taken from Ferguson et al. (14).

Figure 6 plots the contrast between the rods and background for each of the six triangular segments in the Derenzo phantom and the recovery coefficients as a function of rod size in the NEMA image quality phantom. Additional imaging performance metrics comparisons between radionuclides for different reconstruction algorithms are included in supplemental Figure 5.  $^{133}\text{La}$  exhibits similar contrast to  $^{89}\text{Zr}$  and is superior to  $^{68}\text{Ga}$  and  $^{44}\text{Sc}$  for larger rod diameters.  $^{132}\text{La}$  was not included in the contrast comparison due to the low contrast for each rod diameter. The rods could not be distinguished below 1.25 mm diameter for higher energy positron emitters  $^{44}\text{Sc}$  and  $^{68}\text{Ga}$ , and 1 mm for the lower energy positron emitters  $^{18}\text{F}$  and  $^{64}\text{Cu}$ . This blurring is due to the extrinsic scanner resolution, which is significantly impacted by the positron energy and therefore range. The RC comparison demonstrates that  $^{133}\text{La}$  exhibits favorable performance compared to  $^{68}\text{Ga}$  and  $^{132}\text{La}$ .



**FIGURE 6.** (A) Normalized contrast as a function of rod size for different radionuclides in the Derenzo phantom. (B) Impact of radionuclide and reconstruction method on measured recovery coefficients in the NEMA image quality phantom.  $^{18}\text{F}$ ,  $^{64}\text{Cu}$ ,  $^{44}\text{Sc}$  and  $^{68}\text{Ga}$  data were taken from Ferguson et al. (14).

## Radiolabeling

Radiolabeling was performed at 90°C for 30 min and analyzed with radio-TLC using 0.1 M citric acid buffer as the mobile phase. The  $^{133}\text{La}$ -DOTA,  $^{133}\text{La}$ -PSMA-I&T, and  $^{133}\text{La}$ -macropa complexes remained close to the TLC baseline ( $R_f$  0.1–0.2) while unreacted  $^{133}\text{La}$  migrated toward the solvent front ( $R_f$  0.9–1.0). Titration of  $^{133}\text{LaCl}_3$  ( $n=3$ ) yielded an apparent molar activity of  $130 \pm 15$  GBq/ $\mu\text{mol}$  with DOTA,  $73 \pm 18$  GBq/ $\mu\text{mol}$  with PSMA-I&T, and  $206 \pm 31$  GBq/ $\mu\text{mol}$  with macropa.

## Preclinical PET Imaging

Figure 7 depicts static PET images of LNCaP tumor bearing mice 60 min after injection of 33-50 MBq of  $^{133}\text{La}$ -PSMA-I&T (n=4). Tumor uptake was significant, reaching  $\text{SUV}_{\text{mean}}$  of  $0.97 \pm 0.17$  after 60 min. The  $\text{SUV}_{\text{mean}}$  for muscle was  $0.05 \pm 0.01$ , resulting in a tumor-to-muscle ratio (TMR) of  $22.4 \pm 4.5$ . Mice pre-dosed with  $300 \mu\text{g}$  DCFPyL 5 min prior to  $^{133}\text{La}$ -PSMA-I&T injection exhibited significant tumor blocking, with a tumor  $\text{SUV}_{\text{mean}}$  of  $0.11 \pm 0.01$  after 60 min. Most other radioactivity was excreted into the kidneys and urinary bladder.

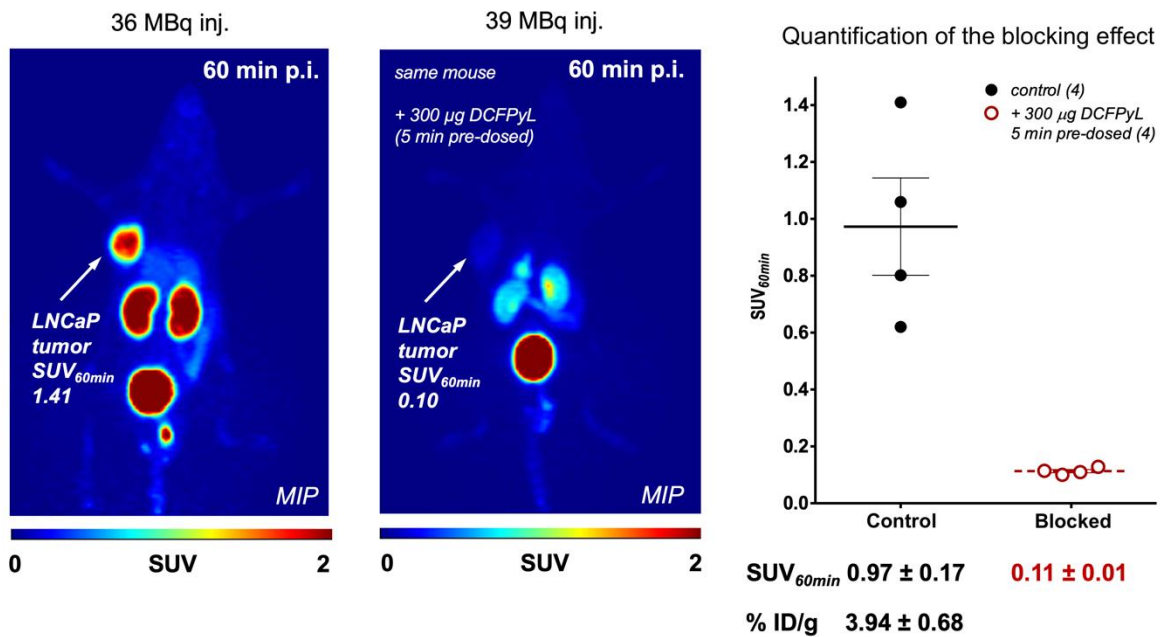


**FIGURE 7.** Representative PET images (MIP - maximum intensity projection) at 60 min of  $^{133}\text{La}$ -PSMA-I&T with and without pre-dose of DCFPyL in LNCaP tumor-bearing mice.

## DISCUSSION

This study presents A) cyclotron production of  $^{133}\text{La}$  using natural and isotopically enriched barium target material, B) favorable fundamental PET phantom imaging characteristics of  $^{133}\text{La}$ , and C) the first *in vivo* preclinical PET tumor imaging using  $^{133}\text{La}$ -PSMA-I&T.

The new target assembly is well suited to the irradiation and processing of Ba metal and  $\text{BaCO}_3$  target material. Using aluminum instead of silver target backings as used in previous studies (3,11) avoids production of long-lived  $^{107}\text{Cd}$ ,  $^{109}\text{Cd}$ , and  $^{106\text{m}}\text{Ag}$ , thereby strongly reducing overall activation of the target, lowering operator exposure and enabling rapid reuse. Using the target backing as an intrinsic degrader simplifies and enhances the available range of irradiation energies. The indium wire seal stayed 1-2 mm outside of the target beam spot, avoiding activation and formation of radiotin isotopes. Sonicating used target discs in 18 M $\Omega$ -cm water allowed repeated reuse to make additional targets, with the same seal and target backing reused over 5 times.

Irradiating enriched  $^{135}\text{BaCO}_3$  at 23.3 MeV produced far more  $^{133}\text{La}$  compared to other target materials, which allows production of clinically relevant  $^{133}\text{La}$  activities with significantly shorter irradiation times than using  $^{\text{nat}}\text{Ba}$  target material. Target separation gave a high  $^{133}\text{LaCl}_3$  yield in a 1 mL product volume, ready for radiolabeling.

Recovery of  $\text{BaCO}_3$  target material demonstrated feasibility for cost-effective recovery of expensive isotopically enriched  $^{135}\text{BaCO}_3$ . XRD analysis of recovered  $\text{BaCO}_3$  showed complete conversion of the  $\text{BaC}_2\text{O}_4$  intermediate and a pure recovered product, validating target material recovery and highlighting the potential for substantially improved economics with a simple and inexpensive recovery process. Radiolabeling DOTA, PSMA-I&T, and macropa with  $^{133}\text{La}$

achieved high apparent molar activities for fresh and recovered BaCO<sub>3</sub> target material, similar to radiolanthanum chelation in previous studies (3,4,5,16).

Using isotopically enriched <sup>135</sup>BaCO<sub>3</sub> target material permits selective production of <sup>133</sup>La and <sup>135</sup>La compared to <sup>nat</sup>Ba target material. Performing irradiations at energies of 23.3 MeV or higher significantly increases <sup>133</sup>La production via the <sup>135</sup>Ba(p,3n)<sup>133</sup>La reaction and reduces <sup>135</sup>La production from the <sup>135</sup>Ba(p,n)<sup>135</sup>La reaction, which is ideal for PET imaging applications. Irradiating at 11.9 MeV with enriched <sup>135</sup>BaCO<sub>3</sub> is ideal for producing large activities of pure <sup>135</sup>La for AET. Utilizing these two distinct reactions permits production of a variety of <sup>133/135</sup>La isotopic blends on variable energy cyclotron.

Another production route could utilize isotopically enriched <sup>134</sup>BaCO<sub>3</sub> target material to produce <sup>133</sup>La via the <sup>134</sup>Ba(p,2n)<sup>133</sup>La reaction. This would enable <sup>133</sup>La production on lower energy cyclotrons owing to the <sup>134</sup>Ba(p,2n)<sup>133</sup>La cross section threshold at 12 MeV as opposed to the 20 MeV threshold for the <sup>135</sup>Ba(p,3n)<sup>133</sup>La reaction. The lower natural isotopic abundance of <sup>134</sup>Ba (2.4%) compared to <sup>135</sup>Ba (6.6%) would result in a higher isotopic enrichment cost. However, this is a compelling option for PET centers with lower energy cyclotrons owing to the 95.4% recovery yield of BaCO<sub>3</sub> target material demonstrated in this study.

PET phantom imaging clearly showed that <sup>133</sup>La exhibits superior spatial resolution and contrast versus <sup>44</sup>Sc, <sup>68</sup>Ga, <sup>132</sup>La, but similar to <sup>89</sup>Zr. As expected, lower positron emission energy leads to improved spatial resolution (17) and results in superior image quality of <sup>133</sup>La versus <sup>132</sup>La, <sup>68</sup>Ga, and <sup>44</sup>Sc. This is clearly translated to preclinical imaging, as evidenced by high spatial resolution. Even with the lower positron branching ratio of <sup>133</sup>La (7.2%) versus other PET radionuclides (96.7% <sup>18</sup>F, 88.9% <sup>68</sup>Ga, 41.2% <sup>132</sup>La), the LNCaP tumor was clearly defined, reaching SUV<sub>mean</sub> of 0.97 ± 0.17 or 3.94 ± 0.68 %ID/g at 60 min p.i.. For <sup>68</sup>Ga-PSMA-I&T,

$4.95 \pm 1.47\%$  ID/g uptake into LNCaP tumors was reported in an *ex vivo* biodistribution (18). As discussed in (3), *in vivo* studies involving retention and dose of  $^{133}\text{La}$  decay daughter  $^{133}\text{Ba}$  would be useful to address this potential limitation, however as shown by Newton et al. (19) the majority of  $^{133}\text{Ba}$  activity could be expected to be excreted within 10 days after injection.

Since lanthanum and actinium are group 3 elements with similar chemical properties, this highlights  $^{133}\text{La}$  as a very strong candidate to become a clinical PET imaging surrogate for  $^{225}\text{Ac}$  alpha therapy, with superior PET imaging compared to  $^{132}\text{La}$ . As established in this study and (3), compared to  $^{132}\text{La}$ ,  $^{133}\text{La}$  has superior inherent cyclotron production characteristics, a lower positron energy that translates to a higher spatial resolution, and lower energy and abundance gamma emissions that would translate to a lower patient and operator dose. This proposes that  $^{133}\text{La}$  represents an attractive candidate for diagnostic PET imaging and treatment monitoring of clinical  $^{225}\text{Ac}$  TAT and research involving  $^{135}\text{La}$  AET.

## CONCLUSIONS

This work demonstrates the strong potential of  $^{133}\text{La}$  to serve as a theranostic PET imaging agent with  $^{225}\text{Ac}$  TAT or  $^{135}\text{La}$  AET. First preclinical *in vivo* PET imaging in LNCaP tumors resulted in high spatial resolution and contrast. Phantom imaging of  $^{133}\text{La}$  demonstrated superior fundamental PET imaging properties including spatial resolution, contrast, and RC compared to other PET radiometals such as  $^{68}\text{Ga}$ ,  $^{44}\text{Sc}$ , and  $^{132}\text{La}$ , and similar properties to  $^{89}\text{Zr}$ . With cyclotron production routes capable of producing clinically relevant  $^{133}\text{La}$  activities, and demonstrated feasibility to perform high-yield recovery of expensive isotopically enriched  $^{135}\text{BaCO}_3$  target material,  $^{133}\text{La}$  appears to be a promising radiometal candidate to provide high resolution PET imaging as a PET/TAT theranostic pair with  $^{225}\text{Ac}$ , or a PET/AET theranostic pair with  $^{135}\text{La}$ .

## **DISCLOSURE**

The authors declare that no competing interests exist.

## **ACKNOWLEDGMENTS**

The authors thank Jonathan Doupe (Alberta Health Services) for guidance throughout cyclotron production, Samantha Leier (Dept. of Oncology) for preparing  $^{89}\text{Zr}$  for phantom imaging, and Rebecca Funk (Dep. of Earth and Atmospheric Sciences) for performing XRD data collection. We thank the Dianne and Irving Kipnes Foundation for supporting this work. B.N. thanks Alberta Advanced Education and the Natural Sciences and Engineering Research Council of Canada for graduate scholarship funding.

## KEY POINTS

**Question:** Is the positron emitter  $^{133}\text{La}$  suitable for *in vivo* tumor imaging, and how do its production techniques and fundamental imaging characteristics compare to other PET radionuclides?

**Pertinent findings:** Phantom imaging showed PET spatial resolution of  $^{133}\text{La}$  to be superior to that of  $^{68}\text{Ga}$ ,  $^{44}\text{Sc}$ ,  $^{132}\text{La}$ , and comparable to  $^{89}\text{Zr}$ . Preclinical imaging with  $^{133}\text{La}$ -PSMA-I&T in tumor-bearing mice clearly delineated tumors with high spatial resolution. Robust, economical, high yield cyclotron  $^{133}\text{La}$  production was demonstrated using recoverable isotopically enriched  $^{135}\text{BaCO}_3$  target material.

**Implications for patient care:** This study shows that  $^{133}\text{La}$  is a strong candidate to improve patient care by providing PET imaging of tumors as a theranostic pair to  $^{225}\text{Ac}$  targeted alpha therapy or potential  $^{135}\text{La}$  Auger electron therapy.

## REFERENCES

1. Velikyan I. Molecular imaging and radiotherapy: theranostics for personalized patient management. *Theranostics*. 2012;2:424-426.
2. Nelson BJB, Andersson JD, Wuest F. Targeted alpha therapy: progress in radionuclide production, radiochemistry, and applications. *Pharmaceutics*. 2020;13:E49.
3. Nelson BJB, Wilson J, Andersson JD, Wuest F. High yield cyclotron production of a novel  $^{133/135}\text{La}$  theranostic pair for nuclear medicine. *Sci Rep*. 2020;10:22203.
4. Aluicio-Sarduy E, Hernandez R, Olson AP, et al. Production and in vivo PET/CT imaging of the theranostic pair  $^{132/135}\text{La}$ . *Sci Rep*. 2019;9:10658.
5. Aluicio-Sarduy E, Thiele NA, Martin KE, et al. Establishing radiolanthanum chemistry for targeted nuclear medicine applications. *Chem Eur J*. 2020;26:1238-1242.
6. Aluicio-Sarduy E, Barnhart TE, Weichert J, Hernandez R, Engle JW. Cyclotron produced  $^{132}\text{La}$  as a PET imaging surrogate of therapeutic  $^{225}\text{Ac}$ . *J Nucl Med*. 2020;jnumed.120.255794.
7. Bailey TA, Mocko V, Shield KM, et al. Developing the  $^{134}\text{Ce}$  and  $^{134}\text{La}$  pair as companion positron emission tomography diagnostic isotopes for  $^{225}\text{Ac}$  and  $^{227}\text{Th}$  radiotherapeutics. *Nat Chem*. 2021;13:284-289.
8. Kratochwil C, Bruchertseifer F, Giesel FL, et al.  $^{225}\text{Ac}$ -PSMA-617 for PSMA-targeted  $\alpha$ -radiation therapy of metastatic castration-resistant prostate cancer. *J Nucl Med*. 2016;57:1941-1944.
9. Sonzogni, A. and Shu, B., 2020. Nudat 2.8 (Nuclear Structure And Decay Data). [online] Nndc.bnl.gov. Available at: <<https://www.nndc.bnl.gov/nudat2/reCenter.jsp?z=56&n=77>> [Accessed 8 September 2020].

10. Rochman D, Koning AJ, Sublet JC, et al. The TENDL library: hope, reality and future. Proceedings of the International Conference on Nuclear Data for Science and Technology; 2016. p. 146.
11. Nelson BJB, Wilson J, Richter S, Duke MJM, Wuest M, Wuest F. Taking cyclotron  $^{68}\text{Ga}$  production to the next level: Expeditious solid target production of  $^{68}\text{Ga}$  for preparation of radiotracers. *Nucl Med Biol.* 2020;80-81:24-31.
12. Ziegler JF, Ziegler MD, Biersack JP, 2009. The stopping and range of ions in matter (SRIM code, version 2013.00). <<http://www.srim.org/>> [Accessed 20 September 2020].
13. Bhatti AS, Dollimore D, Armstrong B. The thermal decomposition of oxalates. Part 19. The thermal decomposition of barium oxalate hemihydrates. *Thermochim Acta.* 1984;79:217-230.
14. Ferguson S, Jans HS, Wuest M, Riauka T, Wuest F. Comparison of scandium-44 g with other PET radionuclides in pre-clinical PET phantom imaging. *EJNMMI Phys.* 2019;6:23.
15. Gates-Rector S, Blanton T. The Powder Diffraction File: a quality materials characterization database. *Powder Diffr.* 2019;34:352-360.
16. Fonslet J, Lee BQ, Tran TA, et al.  $^{135}\text{La}$  as an Auger-electron emitter for targeted internal radiotherapy. *Phys Med Biol.* 2017;63:015026.
17. Levin CS, Hoffman EJ. Calculation of positron range and its effect on the fundamental limit of positron emission tomography system spatial resolution. *Phys Med Biol.* 1999;44:781.
18. Weineisen M, Schottelius M, Simecek J, et al. (2015)  $^{68}\text{Ga}$ - and  $^{177}\text{Lu}$ -Labeled PSMA I&T: Optimization of a PSMA-targeted theranostic concept and first proof-of-concept human studies. *J Nucl Med.* 2015;56:1169-1176.

19. Newton D, Ancill AK, Naylor KE, et al. Long-term retention of injected barium-133 in man. *Radiat Prot Dosim.* 2001;97:231-240.

**TABLE 1**

Isotopic composition of natural and isotopically enriched barium target materials.

Target material	<sup>138</sup> Ba (%)	<sup>137</sup> Ba (%)	<sup>136</sup> Ba (%)	<sup>135</sup> Ba (%)	<sup>134</sup> Ba (%)	<sup>132</sup> Ba (%)	<sup>130</sup> Ba (%)
<sup>nat</sup> BaCO <sub>3</sub> / <sup>nat</sup> Ba metal	71.7	11.2	7.9	6.6	2.4	0.1	0.1
<sup>135</sup> BaCO <sub>3</sub>	2.6	0.8	3.6	92.7	0.3	<0.05	<0.05

**TABLE 2**

Average experimental (n=3) EOB activities (MBq) and saturated yields (MBq/μA) of  $^{133/135}\text{La}$  for 100 μA·min runs at 11.9 and 23.3 MeV incident energies for different barium target materials. Theoretical EOB activities calculated with TENDL are in parentheses.

Beam energy (MeV)	$^{135}\text{BaCO}_3$ target yields		$^{\text{nat}}\text{BaCO}_3$ target yields		$^{\text{nat}}\text{Ba}$ metal target yields	
	$^{135}\text{La}$	$^{133}\text{La}$	$^{135}\text{La}$	$^{133}\text{La}$	$^{135}\text{La}$	$^{133}\text{La}$
11.9	$81 \pm 2$ (79)	0	$6.8 \pm 0.4$ (5.9)	0	$9.9 \pm 0.5$ (10)	0
	y=1377 ± 31		y=115 ± 6		y=167 ± 8	
23.3	$28 \pm 1$ (31)	$214 \pm 7$ (279)	$35 \pm 1$ (41)	$59 \pm 2$ (61)	$48 \pm 1$ (61)	$81 \pm 3$ (94)
	y=475 ± 11	y=736 ± 25	y=598 ± 9	y=204 ± 8	y=809 ± 17	y=277 ± 9

y=saturated yield in MBq/μA

**TABLE 3**

ICP-OES analysis (n=3) of  $^{133}\text{LaCl}_3$  produced with different Ba target materials. Data for Ba metal is from Nelson et al. (3).

<b>Metal</b>	<b>Fresh BaCO<sub>3</sub></b>	<b>Recovered BaCO<sub>3</sub></b>	<b>Ba metal</b>
	<b>Elemental Concentration (ppb)</b>	<b>Elemental Concentration (ppb)</b>	<b>Elemental Concentration (ppb)</b>
Zn	$7.4 \pm 1.7$	$5.5 \pm 2.4$	$76 \pm 55$
Fe	$3.2 \pm 0.4$	$2.1 \pm 0.8$	$16.8 \pm 11.7$
Al	$18 \pm 2$	$16 \pm 1$	$37 \pm 19$
Ba	$240 \pm 179$	$128 \pm 108$	$1150 \pm 360$
In	$2.5 \pm 1.2$	$3.9 \pm 1.5$	$3.1 \pm 0.9$
Cu	$5.5 \pm 0.3$	$5.3 \pm 0.1$	$5.3 \pm 0.4$

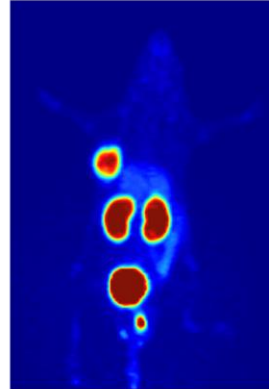
# Graphical Abstract



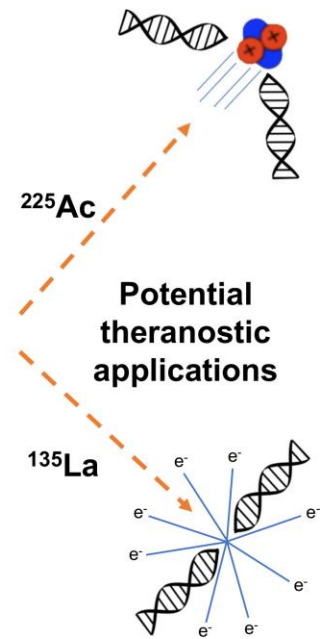
**Cyclotron**  
 **$^{133}\text{La}$  production**



**Radiopharmaceutical**  
**preparation**

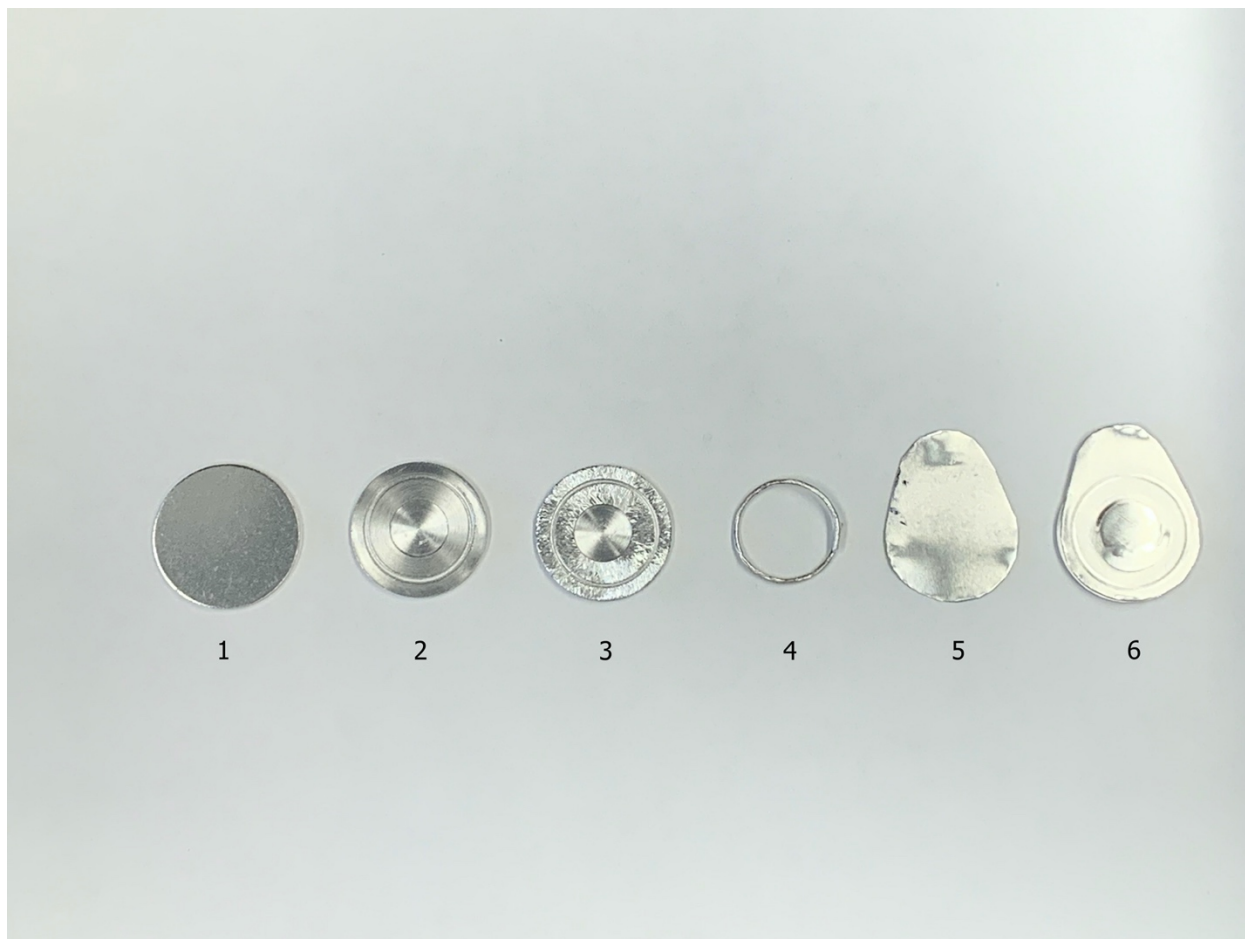


**Preclinical  $^{133}\text{La}$**   
**PET imaging**



## Supplementary Information

### First *in vivo* and phantom imaging of cyclotron produced $^{133}\text{La}$ as a theranostic radionuclide for $^{225}\text{Ac}$ and $^{135}\text{La}$



**Supplemental Figure 1.** Target assembly components. (1) A blank aluminum target disc. (2) A disc machined with a central depression for a target pellet and a groove for the indium wire seal. (3) The front of the machined disc is roughened to facilitate cover attachment. (4) Indium wire seal annulus. (5) Aluminum target cover. (6) Completed target with a  $\text{BaCO}_3$  pellet (not depicted) encapsulated between the aluminum cover and disc.

## XRD Supplementary Material

### X-ray Diffraction Analysis (XRD)

XRD diffractograms were acquired at room temperature on back-packed samples using a Rigaku Ultima IV XRD diffractometer with monochromatic Co K $\alpha$  radiation (1.78886 Å) and an iron filter. The instrument was operated at an accelerating voltage of 38 kV and a current of 38 mA. The patterns were recorded in the 2 $\theta$  range 5° - 90° vs. intensity, at a scan speed of 2°/minute and a step size of 0.0200°.

Data for the most intense eighteen reflections for each sample are listed, in order of decreasing intensity, in Supplemental Tables 1-3 and the background corrected patterns displayed in Supplemental Figures 2-4.

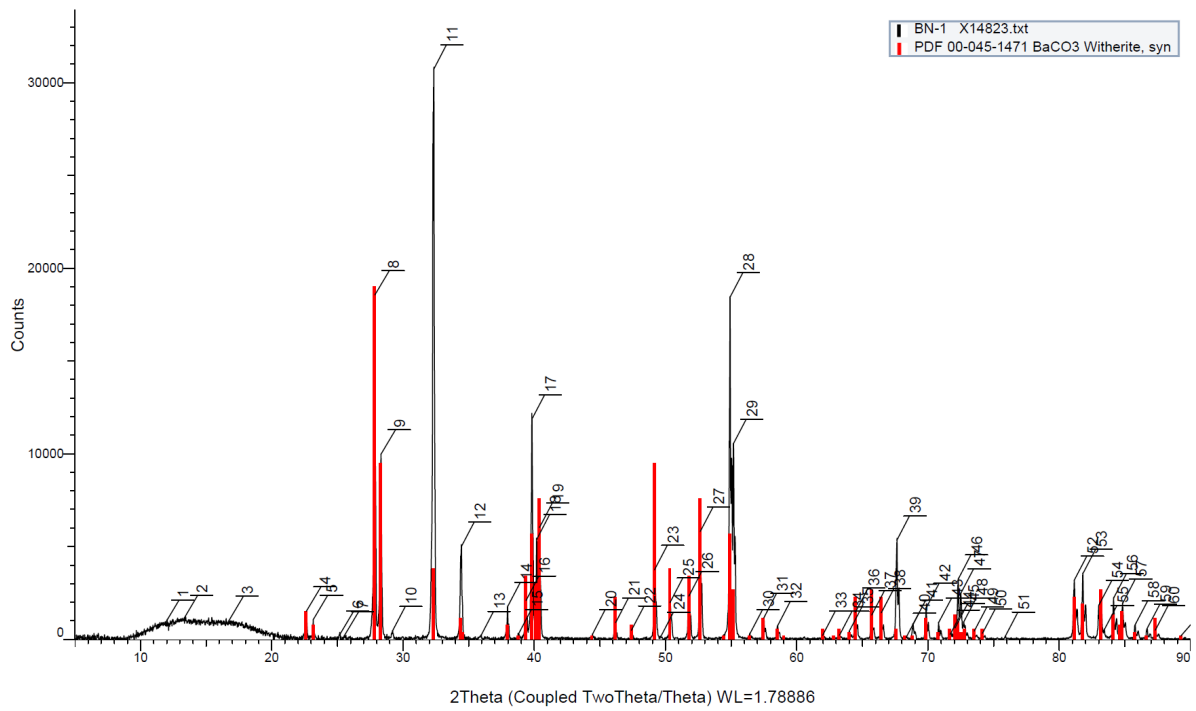
The diffractograms for the Sigma-Aldrich BaCO<sub>3</sub> starting material and recovered BaCO<sub>3</sub> were found to be in very good agreement with the standard lines for Powder Diffraction File PDF 00-045-1451 BaCO<sub>3</sub> Witherite, syn and PDF 01-071-2394 BaCO<sub>3</sub> Witherite, respectively (Gates-Rector, S. D. and Blanton, T. N., 2019). The two BaCO<sub>3</sub> sample XRD patterns (Figures 2 and 4) display 8 major peaks corresponding to d-spacing (Å) values of 3.717, 3.656, 3.214, 2.626, 2.590, 2.148, 2.016 and 1.940 which are respectively indexed as (111), (021), (002), (112), (130), (221), (132) and (113) crystal planes. Differences in the peak intensities for the two BaCO<sub>3</sub> samples are most likely due to preferred crystallite orientation in the case of the Sigma-Aldrich BaCO<sub>3</sub>. The XRD pattern for the recovered BaCO<sub>3</sub> confirms the purity of the material. Powder Diffraction Files 00-037-0674, 00-057-0341 and 00-001-0740 for barium oxalate (Gates-Rector, S. D. and Blanton, T. N., 2019) correspond to the reflections determined for the analyzed BaC<sub>2</sub>O<sub>4</sub> precipitate (Figure 3).

Peak broadening is apparent in the XRD patterns for the precipitated  $\text{BaC}_2\text{O}_4$  and the recovered  $\text{BaCO}_3$  in comparison to the Sigma-Aldrich  $\text{BaCO}_3$  material. Broadening of peaks, also indicated by the full width at half maximum (FWHM) (see Tables 1-3), is a function of crystallite particle size and the degree of crystallinity of a sample and likely indicates the small particle size of the precipitated  $\text{BaC}_2\text{O}_4$  and recovered  $\text{BaCO}_3$ .

**Supplemental Table 1.** XRD results for Sigma-Aldrich BaCO<sub>3</sub> (listed by relative intensity).

<b>Index</b>	<b>2<math>\theta</math> Angle (°)</b>	<b>d Value (Å)</b>	<b>Intensity</b>	<b>Net Int'</b>	<b>Rel Int'</b>	<b>FWHM</b>
11	32.351	3.21072	30713.720	30714	100.00%	0.134
8	27.854	3.71624	18548.040	18548	60.40%	0.124
28	54.920	1.93966	18434.490	18434	60.00%	0.188
17	39.834	2.62558	11862.330	11862	38.60%	0.104
29	55.180	1.93121	10534.340	10534	34.30%	0.262
9	28.320	3.65624	9967.853	9968	32.50%	0.146
19	40.397	2.59053	6011.257	6011	19.60%	0.259
27	52.660	2.01656	5807.729	5808	18.90%	0.143
18	40.188	2.60342	5382.808	5383	17.50%	0.214
12	34.454	3.02011	4994.304	4994	16.30%	0.131
23	49.170	2.14987	3747.903	3748	12.20%	0.189
26	51.790	2.04806	2326.429	2326	7.60%	0.197
16	39.374	2.65502	2086.765	2087	6.80%	0.108
25	50.351	2.10259	1982.291	1982	6.50%	0.171
14	37.978	2.74884	1753.177	1753	5.70%	0.079
4	22.640	4.55674	1508.833	1509	4.90%	0.108
2	13.267	7.74292	1061.780	1062	3.50%	0.160
5	23.159	4.45586	1052.818	1053	3.40%	0.106

(Coupled TwoTheta/Theta)

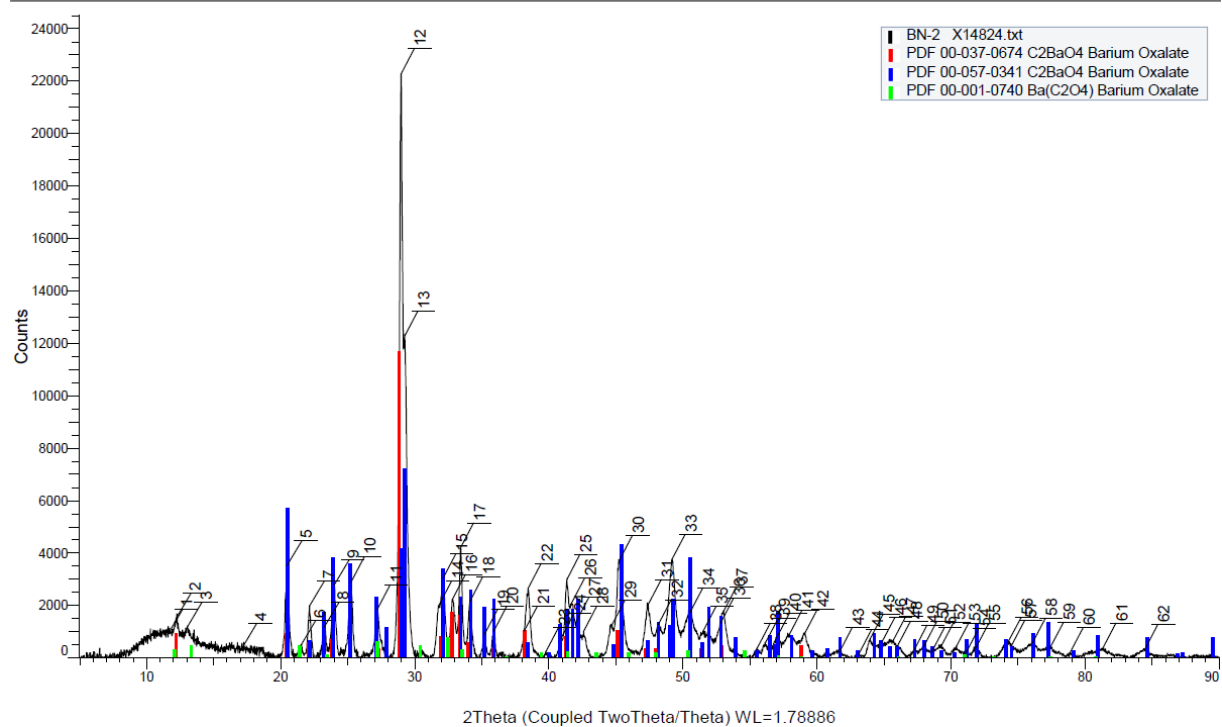


**Supplemental Figure 2.** XRD pattern for Sigma-Aldrich BaCO<sub>3</sub> (Co K $\alpha$ ) with PDF 00-045-1471 BaCO<sub>3</sub> Witherite, syn reflections identified.

**Supplemental Table 2.** XRD results for intermediate BaC<sub>2</sub>O<sub>4</sub> (listed by relative intensity).

<b>Index</b>	<b>2<math>\theta</math> Angle (<math>^{\circ}</math>)</b>	<b>d Value (<math>\text{\AA}</math>)</b>	<b>Intensity</b>	<b>Net Int'</b>	<b>Rel Int'</b>	<b>FWHM</b>
12	28.990	3.57354	22271.370	22271	100.00%	0.445
13	29.255	3.5418	12276.640	12277	55.10%	0.495
17	33.426	3.11022	4198.207	4198	18.90%	0.243
30	45.257	2.32467	3710.984	3711	16.70%	0.424
5	20.466	5.03483	3512.314	3512	15.80%	0.272
15	32.102	3.23494	3022.161	3022	13.60%	0.160
25	41.357	2.53289	2993.660	2994	13.40%	0.160
10	25.260	4.09059	2888.352	2888	13.00%	0.316
9	23.999	4.30212	2779.460	2779	12.50%	0.298
22	38.457	2.71584	2649.232	2649	11.90%	0.377
16	32.817	3.16634	2225.501	2226	10.00%	0.392
18	34.119	3.04887	2143.853	2144	9.60%	0.278
26	41.700	2.51297	2082.546	2083	9.40%	0.160
14	31.791	3.26575	1989.685	1990	8.90%	0.659
7	22.158	4.65454	1981.271	1981	8.90%	0.233
11	27.202	3.80351	1835.502	1836	8.20%	0.333
2	12.215	8.40677	1517.443	1517	6.80%	0.442
27	42.014	2.49507	1344.883	1345	6.00%	0.160

(Coupled TwoTheta/Theta)

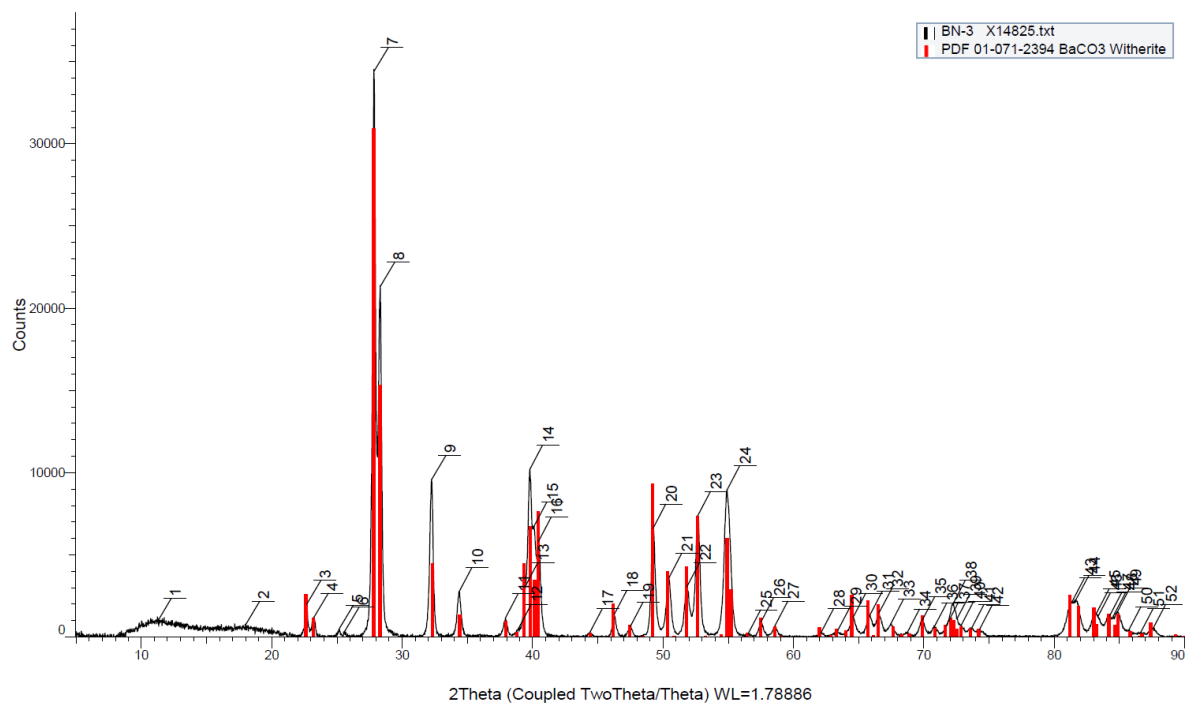


**Supplemental Figure 3.** XRD pattern for  $\text{BaC}_2\text{O}_4$  (Co  $K\alpha$ ) with PDF 00-037-0674, 00-057-0341 and 00-001-0740 Barium oxalate reflections identified.

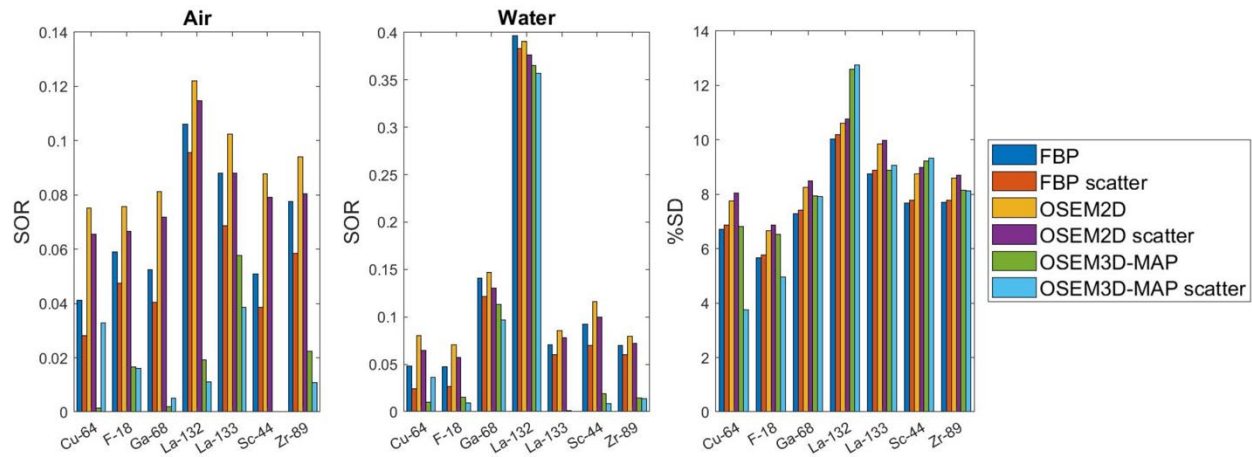
**Supplemental Table 3.** XRD results for recovered BaCO<sub>3</sub> (listed by relative intensity).

Index	2 $\theta$ Angle (°)	d Value (Å)	Intensity	Net Int'	Rel Int'	FWHM
7	27.845	3.71730	34384.680	34385	100.00%	0.259
8	28.318	3.65650	21323.480	21323	62.00%	0.160
14	39.799	2.62783	10191.000	10191	29.60%	0.160
9	32.260	3.21952	9571.121	9571	27.80%	0.281
24	54.907	1.94006	8926.670	8927	26.00%	0.484
23	52.674	2.01608	7369.009	7369	21.40%	0.335
15	40.118	2.60779	6723.588	6724	19.60%	0.160
20	49.236	2.14716	6606.105	6606	19.20%	0.314
16	40.449	2.58728	5804.587	5805	16.90%	0.160
21	50.455	2.09857	3595.132	3595	10.50%	0.357
22	51.832	2.04649	3051.792	3052	8.90%	0.386
13	39.421	2.65198	3027.472	3027	8.80%	0.160
10	34.364	3.02776	2730.448	2730	7.90%	0.317
3	22.675	4.54972	1977.704	1978	5.80%	0.227
18	46.259	2.27702	1362.501	1363	4.00%	0.296
4	23.233	4.44199	1185.054	1185	3.40%	0.284
30	64.577	1.67439	1181.793	1182	3.40%	0.347
11	37.920	2.75290	1157.059	1157	3.40%	0.273

(Coupled TwoTheta/Theta)



**Supplemental Figure 4.** XRD pattern for recovered BaCO<sub>3</sub> (Co K $\alpha$ ) with PDF 01-071-2394 BaCO<sub>3</sub> Witherite reflections identified.



**Supplemental Figure 5.** The impact of radionuclide and reconstruction algorithm on percent standard deviation (%SD) and spill-over ratio (SOR) in air and water. All data were acquired with the same number of counts, using the same method as in Ferguson et al. (2019). Both uncorrected and scatter corrected values are presented. The SOR in air and water was measured using a 4 mm diameter (50% of cylinder diameter) and 7.5-mm-long cylindrical volume of interest in the water- and air-filled inserts. The mean activity ( $C_{\text{cold}}$ ) and standard deviation ( $STD_{\text{cold}}$ ) were calculated in each ROI; the SOR is the ratio of the mean value in the inserts to the mean value of the uniform region, while the uncertainty ( $\sigma_{\text{SOR}}$ ) is calculated using the standard deviation.  $^{18}\text{F}$ ,  $^{64}\text{Cu}$ ,  $^{44}\text{Sc}$  and  $^{68}\text{Ga}$  data were taken from Ferguson et al. (2019).

## References:

1. Gates-Rector S, Blanton T. The Powder Diffraction File: a quality materials characterization database. *Powder Diffr.* 2019;34:352-360.
2. Ferguson S, Jans HS, Wuest M, Riauka T, Wuest F. Comparison of scandium-44 g with other PET radionuclides in pre-clinical PET phantom imaging. *EJNMMI Phys.* 2019;6:23.